

■ Dye-Sensitized Solar Cells | *Hot Paper* |● Non-Covalent Postfunctionalization of Dye Layers on TiO<sub>2</sub> — A Tool for Enhancing Injection in Dye-Sensitized Solar CellsTobias Luchs,<sup>[a]</sup> Anna Zieleniewska,<sup>[b]</sup> Andreas Kunzmann,<sup>[b]</sup> Peter R. Schol,<sup>[b]</sup> Dirk M. Guldi,<sup>\*,[b]</sup> and Andreas Hirsch<sup>\*,[a]</sup>*Dedicated to Professor Luis Echegoyen on the occasion of his 70th anniversary*

**Abstract:** We report on newly tailored dye layers, which were employed, on one hand, for covalent deposition and, on the other hand, for non-covalently post-functionalizing TiO<sub>2</sub> nanoparticle films. Our functionalization concept enabled intermixing a stable covalent attachment of a first layer with a highly versatile and reversible hydrogen bonding through the Hamilton receptor–cyanuric acid binding motif as a second layer. Following this concept, we integrat-

ed step-by-step a first porphyrin layer and a second porphyrin/BODIPY layer. The individual building blocks and their corresponding combinations were probed with regard to their photophysical properties, and the most promising combinations were implemented in dye-sensitized solar cells (DSSCs). Relative to the first porphyrin layer adding the second porphyrin/BODIPY layers increased the overall DSSC efficiency by up to 43 %.


## Introduction


The construction of hybrid architectures starting at nanosized entities and molecular building blocks is a powerful tool towards the development of advanced multifunctional materials.<sup>[1]</sup> Leading examples have made it into applications such as catalysis,<sup>[2]</sup> sensing,<sup>[3]</sup> drug delivery,<sup>[4]</sup> removal of water contaminants,<sup>[5]</sup> and dye sensitized solar cells<sup>[6]</sup> (DSSCs). Potential pathways in terms of realizing such hybrid architectures are manifold and include among many others self-assembly via covalent or non-covalent interactions. Covalent functionalization, for example, has extensively been employed in the context of highly ordered self-assembled monolayers (SAMs).<sup>[7]</sup> This approach has enabled the realization of many functional materials like transistors<sup>[8]</sup> and DSSCs.<sup>[9]</sup> More recently, SAM post-func-

tionalization through covalent modifications has been explored. The most prominent examples rely on nucleophilic substitutions<sup>[10]</sup> or click chemistry, especially the dipolar Huisgen 1,3-cycloaddition to couple azides and acetylenes.<sup>[11]</sup> In contrast to covalent approaches, self-assembly based on non-covalent functionalization supports a high degree of reversibility and versatility.<sup>[12]</sup> Controlled SAM formation based on covalent as well as non-covalent interactions made a series of mixed inorganic–organic nanoparticles with smoothly tunable surface properties accessible.<sup>[13]</sup> The resulting nanoparticles have, for example, been utilized in either removing contaminants from water<sup>[5b]</sup> or in radiation therapy.<sup>[14]</sup> The layer-by-layer technique (LbL), which was first introduced by Decher, is one prominent example of hierarchical architectures, which are solely based on the utilization of non-covalent forces.<sup>[15]</sup> A substrate, for instance, is alternately dipped into solutions of either positively or negatively charged polymers. Hereby, the layered architectures are stabilized through electrostatic interactions. In recent years, this strategy was used for the formation of functional, nanosized architectures by layering tailored molecular building blocks and charged nanoparticles.<sup>[16]</sup> When using H-bonding, stronger binding and higher directionality evolved. Important is the fact that solvents govern the strength of H-bonding and, in turn, the precise control over the reversibility. Similar to the LbL methodology, H-bonding stands out for functionalizing nanomaterials.<sup>[17]</sup> One of the most prominent examples is the Hamilton receptor/cyanuric acid binding motif (Figure 1).<sup>[18]</sup> Its high binding constant in the range from 10<sup>3</sup> to 10<sup>6</sup> L mol<sup>−1</sup> is truly remarkable.<sup>[18a,19]</sup> Not surprisingly, this binding motif enabled the preparation of molecular wires,<sup>[20]</sup> rotaxanes through a H-bonding template,<sup>[21]</sup> attachment to carbon allotropes,<sup>[22]</sup> perylene–fullerene–porphyrin

[a] T. Luchs, Prof. Dr. A. Hirsch  
Chair of Organic Chemistry II, Department of Chemistry & Pharmacy  
Friedrich-Alexander-Universität Erlangen-Nürnberg  
Nikolaus-Fiebiger-Straße 10, 91058 Erlangen (Germany)  
E-mail: andreas.hirsch@fau.de

[b] Dr. A. Zieleniewska, Dr. A. Kunzmann, P. R. Schol, Prof. Dr. D. M. Guldi  
Chair of Physical Chemistry I, Department of Chemistry & Pharmacy  
Friedrich-Alexander-Universität Erlangen  
Egerlandstraße 3, 91058 Erlangen (Germany)  
E-mail: dirk.guldi@fau.de

 Supporting Information and the ORCID identification number(s) for the author(s) of this article can be found under:  
<https://doi.org/10.1002/chem.202004928>.

 © 2021 The Authors. Chemistry - A European Journal published by Wiley-VCH GmbH. This is an open access article under the terms of the Creative Commons Attribution Non-Commercial NoDerivs License, which permits use and distribution in any medium, provided the original work is properly cited, the use is non-commercial and no modifications or adaptations are made.

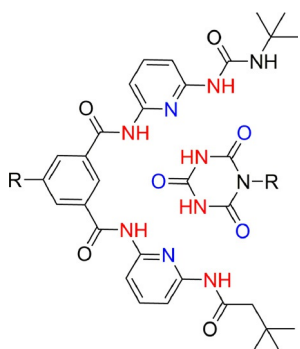


**Figure 1.** Schematic representation of the complementary hydrogen bonding in the Hamilton receptor–cyanuric acid binding motif.

hybrids with a charge-transfer character<sup>[23]</sup> and even the attachment of gold nanoparticles on polymeric surfaces.<sup>[24]</sup>

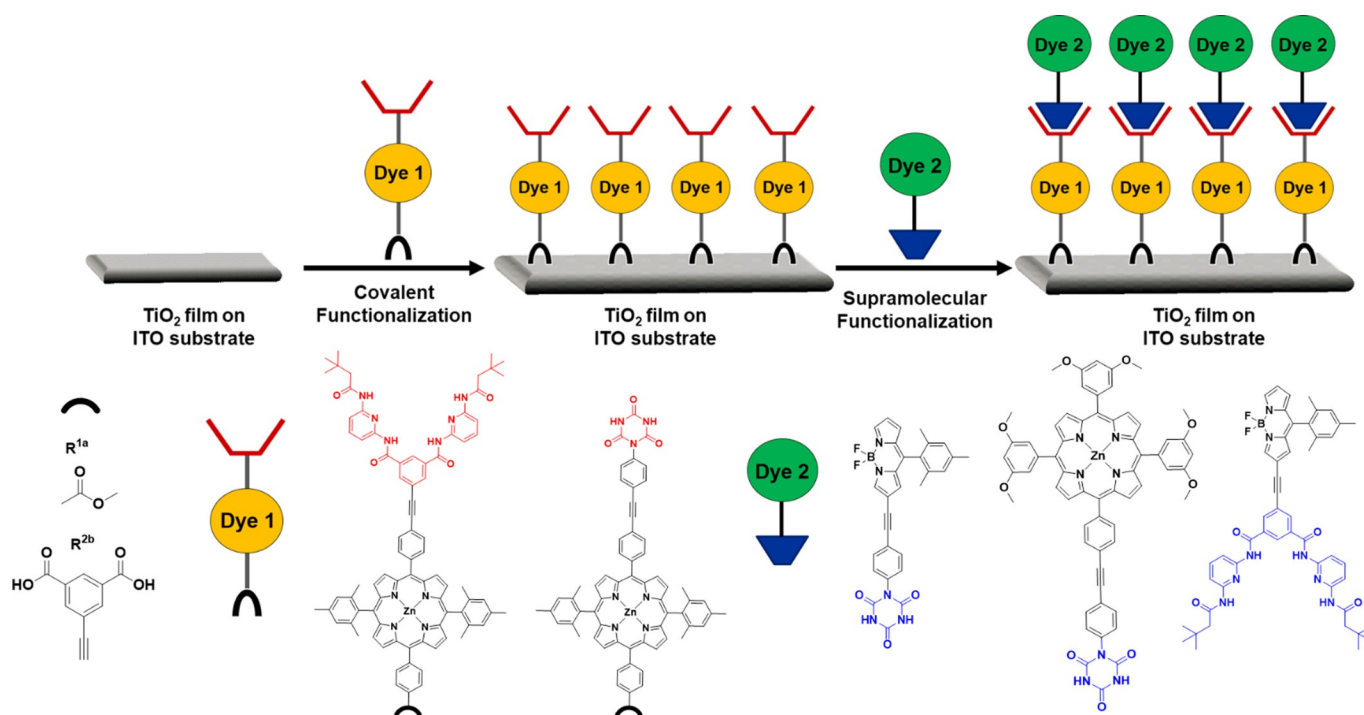
Our research group has taken the aforementioned as a starting point and advanced it by utilizing the Hamilton receptor/cyanuric acid binding motif to integrate tailored organic building blocks onto metal oxide nanoparticles.<sup>[25]</sup> Following such a covalent/non-covalent strategy, reversible superstructures consisting of gold and TiO<sub>2</sub> nanoparticles were held together by H-bonding.<sup>[26]</sup> Through the controlled surface immobilization of a Hamilton receptor featuring carboxylic acids our group also succeeded in the non-covalent orthogonal assembly of a porphyrin–cyanurate onto TiO<sub>2</sub> surfaces. The latter is not only redox but also photoactive and combines the benefits of the first layer functionalization based on covalent surface attachment with the control over the reversibility of the second layer functionalization based on H-bonding.<sup>[27]</sup>

Herein, we report on the controlled deposition of porphyrin–dipyrromethane boron difluoride (BODIPY) and porphyrin–porphyrin bilayers onto the surface of doctor-bladed TiO<sub>2</sub> films via the combination of covalent and non-covalent self-assembly (Scheme 1). Initially, several Hamilton receptor porphyrins and/or porphyrin cyanurates featuring one or two carboxylates as TiO<sub>2</sub> anchors were prepared through multi-step organic syntheses. Furthermore, a series of BODIPY or porphyrin ligands equipped with a complementary supramolecular recognition motif was prepared. In a first step the supramolecular binding, electrochemistry, and photophysical properties of these building blocks were studied in solution. Finally, the binding was transferred from solution onto doctor-bladed TiO<sub>2</sub>-films. In the resulting hierarchical architectures, a first layer, that is, a covalently attached porphyrin, was combined with a second layer, that is, a non-covalently attached porphyrin or BODIPY. Such a sequential coating enables, on one hand, optimizing the DSSC performance through complementing the absorption of a first layer dye by a second layer dye and on the other hand a high degree of versatility through the reversible H-bonding attachment.

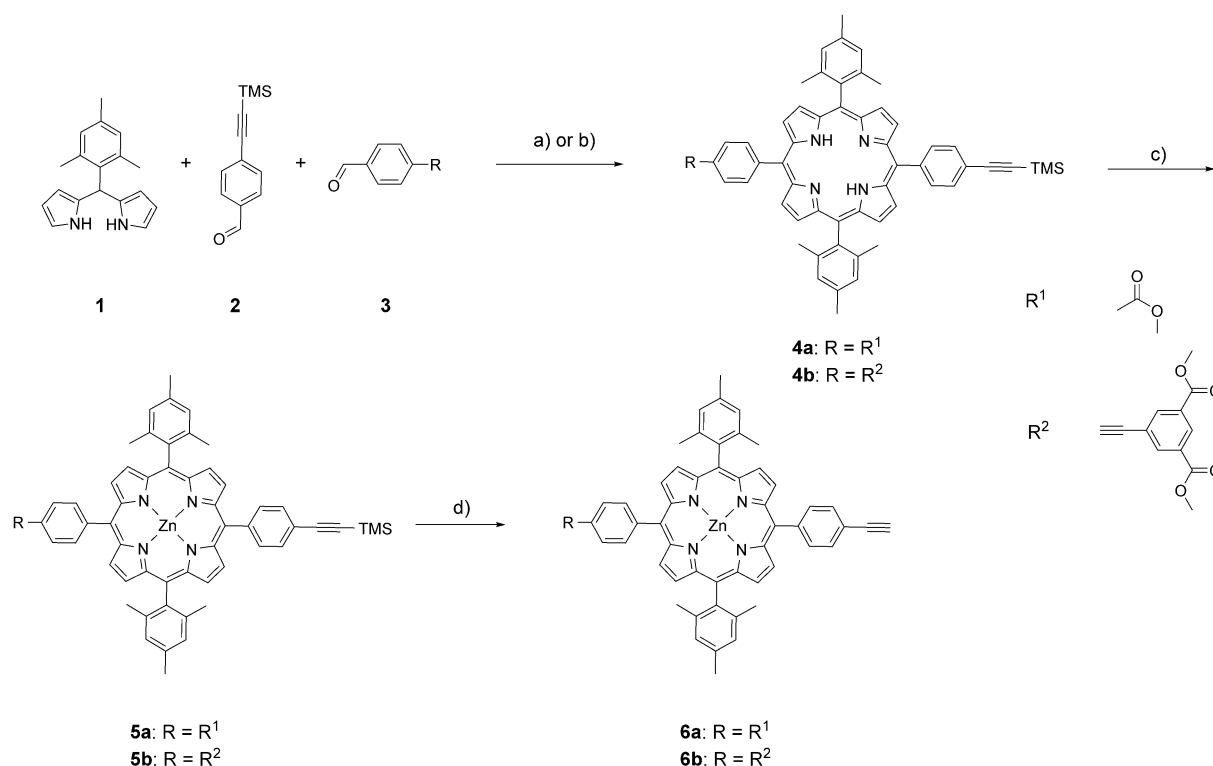
## Results and Discussion

### Synthesis and complexation

We opted for a (metallo)porphyrin as first-layer dye in the DSSCs. As such, the (metallo)porphyrin should feature a suitable TiO<sub>2</sub> anchor, on one hand, and a recognition motif for the post-functionalization by means of H-bonding, on the other hand. Therefore, the synthesis of a *trans*-AB<sub>2</sub>C (metallo)por-



**Scheme 1.** Schematic representation of the step-by-step functionalization of doctor-bladed TiO<sub>2</sub> films with dye 1 and dye 2 by means of covalent and non-covalent methodologies, respectively.



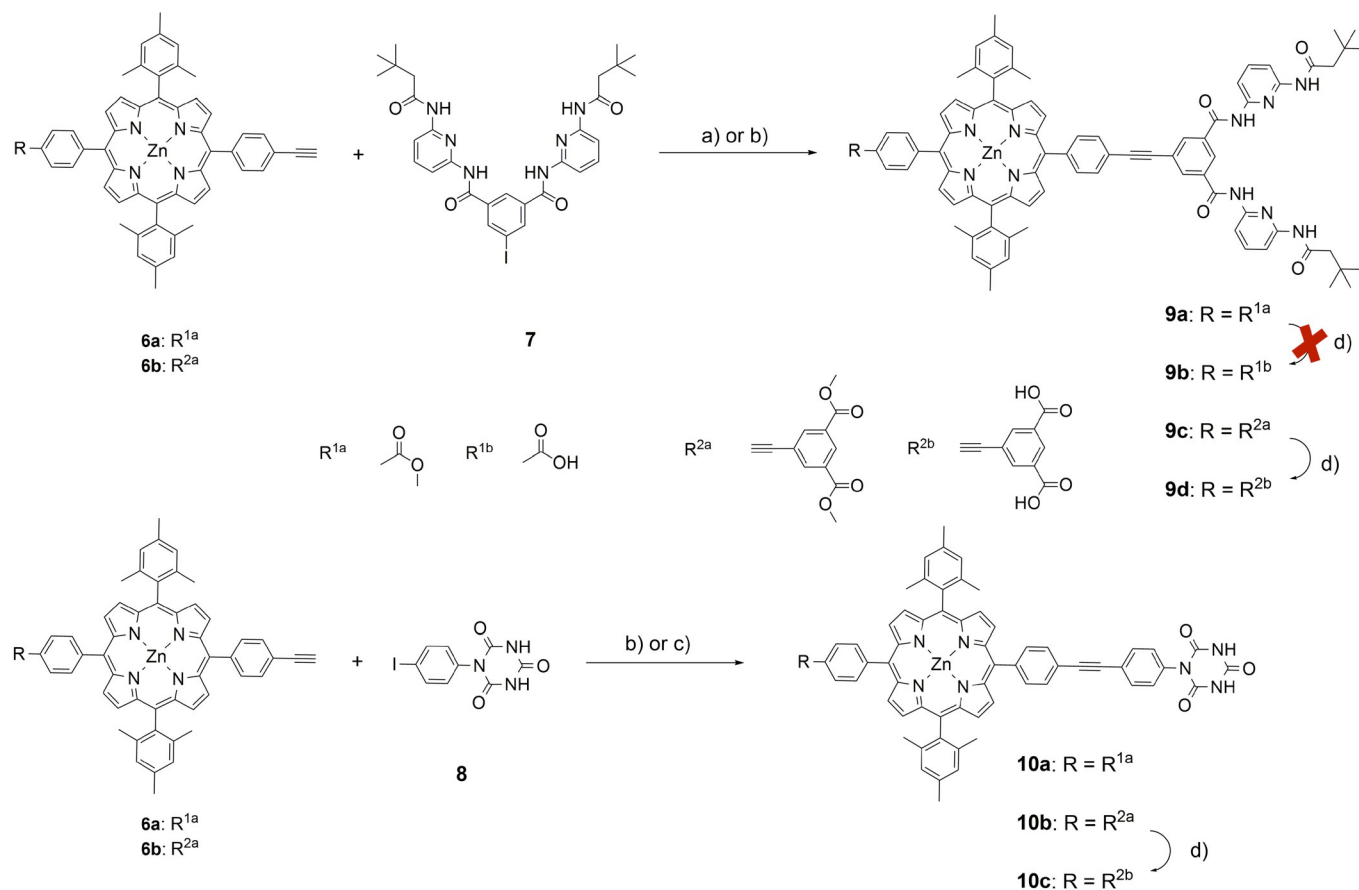
**Scheme 2.** Synthesis of two different *trans*-AB<sub>2</sub>C porphyrins featuring anchor groups for TiO<sub>2</sub> surfaces: a) 0.9 equiv. BF<sub>3</sub>·OEt<sub>2</sub>, 2.8 equiv. DDQ, CHCl<sub>3</sub>, 2 h; b) 0.4 equiv. I<sub>2</sub>, 1.5 equiv. *p*-chloranil, dichloromethane (DCM), 5 min; c) 1.5 equiv. ZnOAc, THF, 2 h; and d) 3 equiv. TBAF, THF, 3 h.

pyrrole carrying either a carboxylic acid ester (R<sup>1</sup>) or an isophthalic acid ester derivative (R<sup>2</sup>) as protected anchors, was conducted (Scheme 2). The (metallo)porphyrin synthesis was carried out in two different ways. For method A, the condensation of mesityl dipyrromethane (**1**), 4-[2-(trimethylsilyl)ethynyl]benzaldehyde (**2**) and benzaldehyde derivative (**3**) was initiated by addition of BF<sub>3</sub>·OEt<sub>2</sub>; after stirring for 2 h the reaction mixture was treated with DDQ (2,3-dichloro-5,6-dicyano-1,4-benzoquinone). In this standard wet chemical approach, the desired *trans*-configured porphyrin was isolated after a single-column chromatographic step in yields of 24% (**4a**) and 14% (**4b**), respectively.

Procedure B was based on utilizing microwave irradiation. In particular, iodine was added to a mixture of dipyrromethane **1** and the aldehyde building blocks **2** and **3** (Scheme 2). The mixture was heated to 40 °C for 5 min using microwave irradiation. This was followed by oxidation with *p*-chloranil. The desired *trans*-AB<sub>2</sub>C porphyrin was obtained after a single column chromatographic step in yields of 22% (**4a**) and 21% (**4b**). Overall, the microwave-based procedure B resulted in significantly shorter reaction times and easier purification. After subsequent metalation with zinc acetate the resulting (metallo)porphyrins were subjected to desilylation using a 1 M solution of TBAF (tetrabutylammonium fluoride) in THF.

Deprotected ethynyl (metallo)porphyrins **6a** and **6b** were obtained in good yields. Next, an iodine-substituted Hamilton receptor (**7**) and an iodine-substituted cyanurate (**8**) were prepared according to literature procedures.<sup>[20a,28]</sup> These building blocks were then coupled to the asymmetric ethynyl (metallo)-

porphyrins in a Sonogashira cross-coupling reaction. In a standard approach, iodo-Hamilton receptor **7** was coupled to ethynyl (metallo)porphyrins **6a** or **6b**, catalyzed by Pd(PPh<sub>3</sub>)<sub>4</sub>, PPh<sub>3</sub>, and NEt<sub>3</sub> under inert conditions. The Hamilton receptor-functionalized (metallo)porphyrins were successfully formed in up to 57% yield (**9a**) after stirring at 80 °C for approximately 3 days. For the preparation of the cyanuric acid-modified (metallo)porphyrin **10a**, microwave syntheses were explored. Ethynyl (metallo)porphyrin **6a** and **8** were treated with catalytic amounts of Pd(PPh<sub>3</sub>)<sub>2</sub>Cl<sub>2</sub>, CuI, and PPh<sub>3</sub> (Scheme 3). After degassing the mixture, it was heated to 150 °C under microwave irradiation. A closer look at the reaction monitoring indicated that an almost complete conversion set in after 32 min. Cyanuric acid-modified (metallo)porphyrin **10a** was obtained in 40% yield after column chromatography. Once again, the preparation of **10b** was carried out under the previously described standard conditions in a yield of 46%. Finally, deprotection of the esters under basic conditions yielded the (metallo)porphyrin building blocks **9d** and **10c** for the first-layer dye. Deprotection of the monocarboxylate ester **9a** to the corresponding carboxylic acid, however, was not possible. The successful deprotection of the esters was verified by means of high-resolution mass spectrometry and NMR spectroscopy. As second layer dye, BODIPYs as well as (metallo)porphyrins were chosen. First, the asymmetrical iodo-BODIPY (**11**) was treated with the ethynyl Hamilton receptor **12** in a Sonogashira reaction to obtain the Hamilton receptor-functionalized BODIPY **15** after a single-column chromatographic step (Scheme 4). Cyanuric acid-functionalized BODIPY **16** was also obtained in a Sonoga-



**Scheme 3.** Synthetic pathway to different AB<sub>2</sub>C porphyrins carrying anchor groups for metal oxide surfaces and a Hamilton receptor or cyanuric acid group for further post-functionalization via hydrogen bonding: a) Pd<sub>2</sub>(dba)<sub>3</sub> (dba = dibenzylidenacetone), AsPh<sub>3</sub>, CuI, THF/NEt<sub>3</sub>, 80 °C, 3 days; b) Pd(PPh<sub>3</sub>)<sub>4</sub>, PPh<sub>3</sub>, CuI, THF/NEt<sub>3</sub>, 80 °C, 3 days; c) Pd(PPh<sub>3</sub>)<sub>2</sub>Cl<sub>2</sub>, PPh<sub>3</sub>, CuI, THF/NEt<sub>3</sub>, 150 °C, 32 min, and d) NaOH, THF, 24 h.

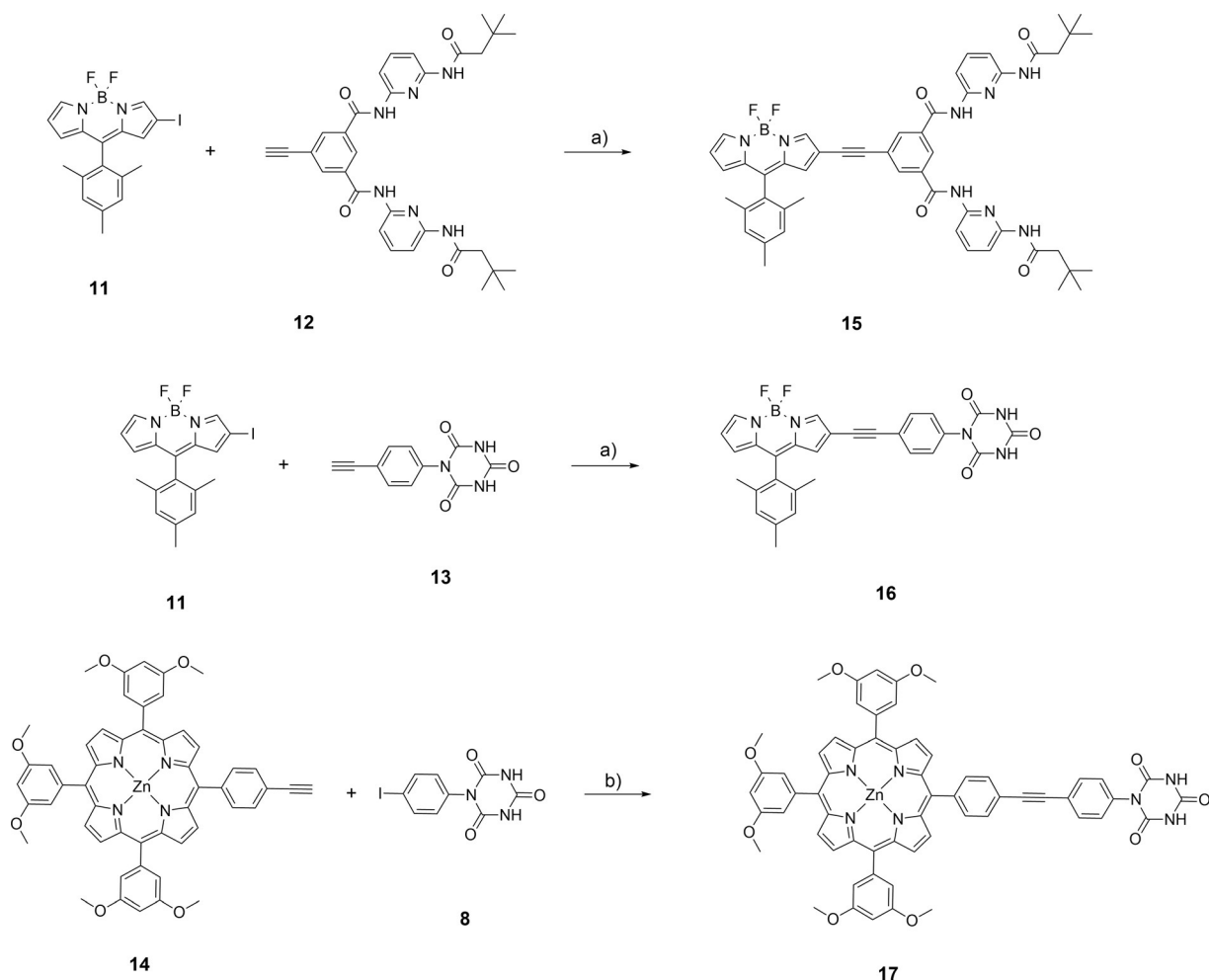
shira reaction of **11** and ethynyl cyanurate (**13**). Several chromatographic steps including reverse-phase HPLC were, however, necessary to purify the crude reaction mixture. Finally, a new microwave-assisted procedure for preparation of the literature-known cyanuric acid (metallo)porphyrin **17** was developed. Ethynyl (metallo)porphyrin **14** and **8** were treated with Pd(PPh<sub>3</sub>)<sub>2</sub>Cl<sub>2</sub> and CuI at 150 °C to obtain **17** in 39% yield. This reduced the reaction time from 3 days to 32 min. To validate the complementary H-bonding capabilities, the specific bindings of the Hamilton receptor/cyanuric acid couples **9a-17** and **10a-15** were investigated by means of <sup>1</sup>H-NMR titrations. The change in the chemical shifts of the amide protons (red dot and purple dot) of the Hamilton receptor prompts to the successful complexation of cyanuric acid through H-bonding (Figures 2 and S25, S26). The binding constants were obtained by plotting the changes in chemical shift of the Hamilton receptor amide protons versus the concentration of cyanuric acid. These plots were then analyzed with the help of the calculator bindfit from supramolecular.org to obtain the corresponding binding constants. For **9a-17** a binding constant of 2.98 × 10<sup>5</sup> L mol<sup>-1</sup> and for **15-10c** a binding constant of 1.74 × 10<sup>4</sup> L mol<sup>-1</sup> was determined. Furthermore, a Jobs plot analysis of the titration data was employed to verify the binding stoi-

chiometry. To this end, the product of the chemical shift variation of the Hamilton receptor amide proton NH1 (red dot) and the molar fraction of the Hamilton receptor (Host) were plotted against the molar fraction of the host (Figures 2 and S25, S26).

In all cases, a maximum at a mole fraction of 0.5 verified the 1:1 binding stoichiometry of the Hamilton receptor/cyanuric acid couples.

### Physicochemical investigations

The absorption spectra of **9d**, **16**, and **9d-16** taken in chloroform are shown in Figure 3. For example, the absorption spectrum of **9d** exhibits signatures typical for (metallo)porphyrins, that is, a strong Soret-band absorption at 427 nm and weaker Q-band absorptions at 554 and 599 nm. In contrast, the absorption spectrum of **16** is dominated by a high energy  $\pi \rightarrow \pi^*$  transitions at 393 nm and a low energy spin-allowed  $\pi \rightarrow \pi^*$  transition at 550 nm.<sup>[29]</sup> A comparison of the absorption spectra taken for **9d-16** with those of **9d** and **16** revealed only minor changes. In particular, the Soret-band absorption of **9d** broadens and the low-energy  $\pi \rightarrow \pi^*$  transition of **16** red-shifts from 543 to 549 nm. A closer look at Figure 3b reveals that all the



**Scheme 4.** Synthesis of several dye molecules with Hamilton receptor or cyanuric acid groups for the supramolecular functionalization of the first dye layers: a)  $\text{Pd}(\text{PPh}_3)_2\text{Cl}_2$ ,  $\text{PPh}_3$ ,  $\text{CuI}$ ,  $\text{THF}/\text{NEt}_3$ , RT, overnight; and b)  $\text{Pd}(\text{PPh}_3)_2\text{Cl}_2$ ,  $\text{PPh}_3$ ,  $\text{CuI}$ ,  $\text{THF}/\text{NET}_3$ ,  $150^\circ\text{C}$ , 32 min.

absorption features further broaden after adsorption on the surface of transparent  $\text{TiO}_2$  films. In solution, BODIPY-related features dominate in the 500–600 nm range of the (metallo)porphyrin-based Q-band signatures in **9d·16**. In the  $\text{TiO}_2$  films, BODIPY-related transitions at 523 nm are only clearly discernable in **9d·16**, but they do not dominate.

**9d**, **16**, and **9d·16** were also studied using steady-state fluorescence spectroscopy at room temperature (Figure S29). **9d** exhibits the characteristic fluorescence of (metallo)porphyrins, namely maxima at 610 and 656 nm. For **16**, we note an intense fluorescence, which maximizes at 582 nm. Selective 506 nm photoexcitation of BODIPY in **9d·16** shows exclusively the fluorescence that relate to BODIPY (Figure S29a). These results suggest that BODIPY in **9d·16** has little or no effect on the fluorescence of **9d**. The overlapping fluorescence of **9d** and **16** render, however, an unambiguous analysis rather difficult. Analogous observations have been made with **10c**, **15**, and **10c·15** in the steady-state absorption and fluorescence measurements (Figure S30).

To elucidate the processes taking place upon photoexcitation, transient absorption spectroscopy (TAS) measurements were performed both in solution and on semiconducting elec-

trodes in the presence of the electrolyte. The experiments were conducted for **9d**, **16**, and **9d·16** as well as for **10c**, **15**, and **10c·15**, in a solvent mixture of THF/acetonitrile (ACN) (1:1 v/v). Time-dependent excited-state features and kinetics thereof were evaluated by means of multiwavelength analysis to corroborate the mechanism, by which charges are injected into  $\text{TiO}_2$  (vide infra).

Those experiments, which were conducted in solution, serve as reference. In the solvent mixture, 430 nm photoexcitation of either **9d** or **10c** commences with the formation of transient absorption spectra, which include 457, 604, and 657 nm minima and 461, 580, 635, and 1278 nm maxima, which dominate the fs-TAS dynamics (Figures S31 and S34 in the Supporting Information). The 457 nm minimum is due to ground-state bleaching of the Q-band absorption whereas the 603 and 657 nm minima are due to stimulated fluorescence. These transform into triplet-excited state features located at 450 and 840 nm within 1380 ps.

In solution, no appreciable changes are observed neither in **9d·16** nor in **10c·15** (Figures S33 and S36). Similar to the steady-state fluorescence experiments, we failed to gather evidence for any energy transfer from the (metallo)porphyrins to



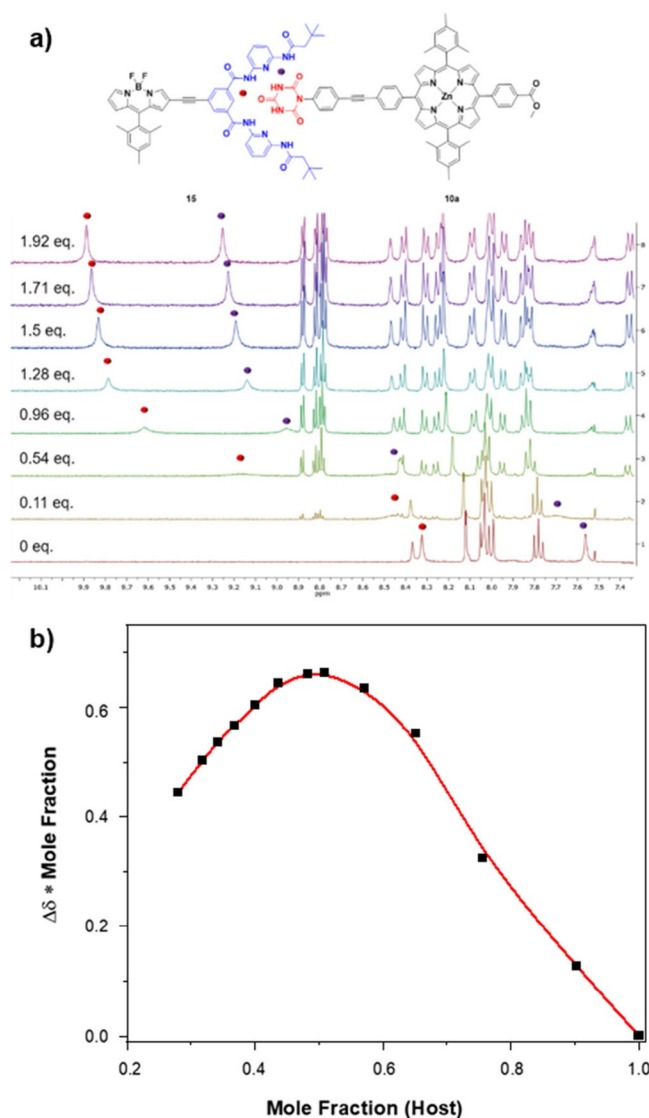


**Figure 2.** a)  $^1\text{H}$  NMR titration of Hamilton receptor **15** with several equivalents of cyanuric acid porphyrin **10c** ( $\text{CDCl}_3/\text{CD}_2\text{Cl}_2$ , 400 MHz). b) Job's plot of the NMR titration data of complex **15-10c**.

BODIPY. Instead, the differential absorption spectra look exactly like those recorded for (metallo)porphyrins **9d** and **10c**. Importantly, excitation of either **15** or **16** at 430 nm results in differential absorption spectra typical for BODIPYs, that is, minima at 532 and 610 nm (Figures S32 and S35). In essence, the lack of BODIPY-related features upon 430 nm photoexcitation of **9d-16** or **10c-15** is not a result of selective (metallo)porphyrin excitation.

The picture changes once **9d**, **16**, and **9d-16** as well as **10c**, **15**, and **10c-15** are deposited on 9  $\mu\text{m}$ -thick  $\text{TiO}_2$  films in the presence of an electrolyte:  $\text{TiO}_2\text{-9d-16}$  and  $\text{TiO}_2\text{-10c-15}$ . Upon 430 nm excitation of **9d** and **10c**, they both show the instantaneous formation of the one-electron oxidized form of the (metallo)porphyrin (Figures S36 and S37). Most notable is the lack of stimulated fluorescence, on one hand, and 538 and 850 nm maxima, on the other hand. The maxima are in sound agreement with those detected upon spectro-electrochemical

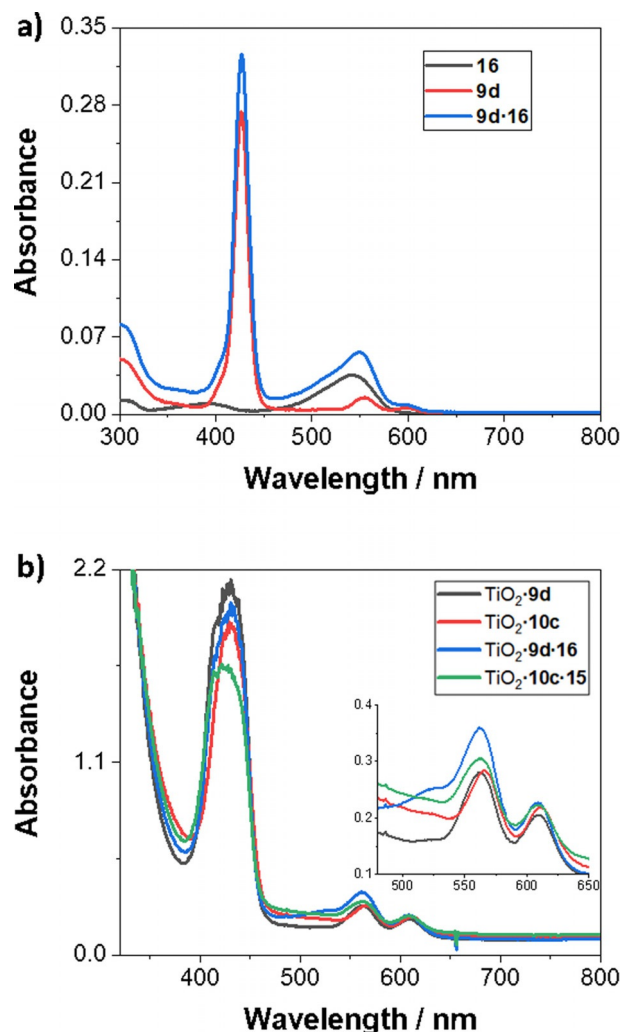


**Figure 3.** a) Steady-state absorption spectra of **16**, **9d**, and **9d-16** (1:1 ratio) in chloroform. b) Steady-state absorption spectra of  $\text{TiO}_2\text{-9d}$ ,  $\text{TiO}_2\text{-10c}$ ,  $\text{TiO}_2\text{-9d-16}$ , and  $\text{TiO}_2\text{-10c-15}$  with electrolyte.

oxidation of, for example, **9d** (Figure S44). Based on the multi-wavelength analysis, the charge injection kinetics are best described by three components.

In all cases, an ultrafast component, deconvolution of which is limited by the instrument response, is implied. The failure to detect this component, when 610 nm is used as excitation wavelength (Figures S41 and S43) rather than 430 nm, suggests that the latter is likely to be charge injection from the second singlet excited state ( $S_2$ ). Taking into consideration that the transient absorption spectra upon 610 nm excitation features contributions from the first singlet excited state ( $S_1$ ) and the one-electron oxidized form of the (metallo)porphyrin, it is fair to assume that upon 430 nm photoexcitation the majority of charge injection evolves from the  $S_2$  state. The ultrafast charge injection stemming from  $S_2$  is followed by two slower components. The faster of them, that is, the second one, takes around 5.6 and 2.47 ps in the cases of **9d** and **10c**, respectively. As the same lifetimes are also discernible upon 610 nm excitation it is very likely that this process is a charge injection from the  $S_1$  state. The slower of them, that is, the third one

takes 227 ps for **9d** and 308 ps for **10c**. Based on the literature and also considering the red-shifts of the transient absorption features in the 660 to 685 nm region, the third component is assigned with confidence to charges that are injected into non-mobile surface states, which undergo thermal relaxation into the conduction band.<sup>[30]</sup>

Changes were noted in the transient absorption spectra of  $\text{TiO}_2$ -**9d-16** (Figure 4). In addition to the one-electron oxidized form of the (metallo)porphyrin **9d** broadening of the ground state bleaching is observed at around 565 nm. The latter is in sound agreement with the BODIPY signatures. Considering the lack of comparable observations in the solution studies, the evolving features are not a result of energy transfer processes

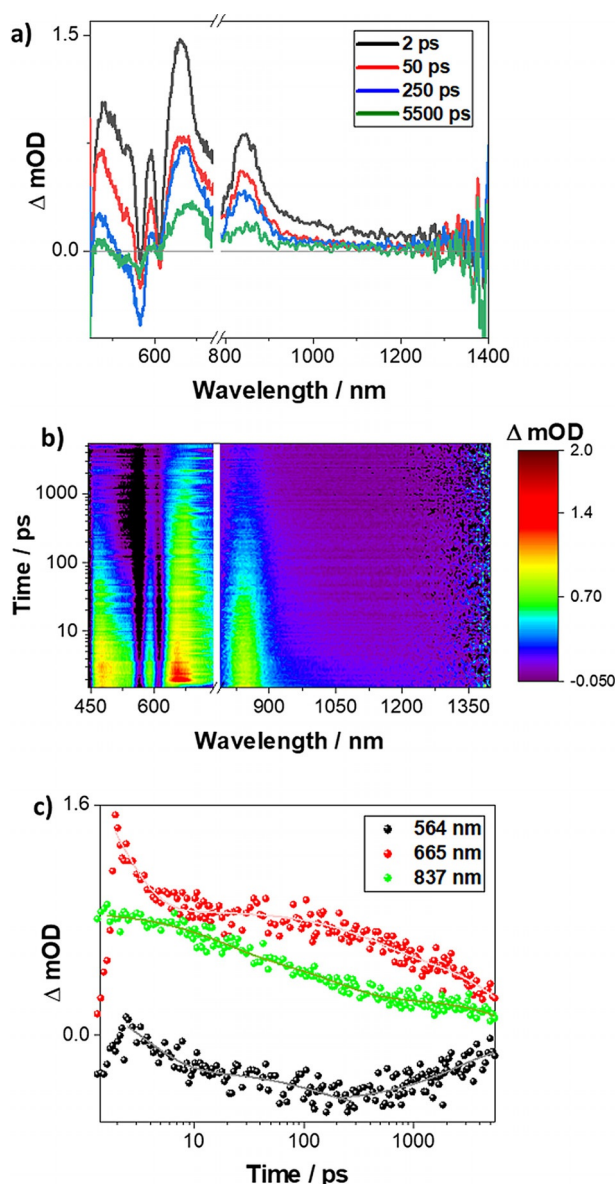


**Figure 4.** a) Differential absorption spectra with the depicted time delays and b) 3D representation of differential absorption spectra (visible and near-infrared) obtained upon femtosecond flash photolysis (430 nm) of  $\text{TiO}_2$ -**9d-16** with electrolyte with several time delays between 0 and 5500 ps at room temperature. c) Time absorption profiles of the spectra at 564, 665, and 837 nm.

but are rather related to a charge transfer. To gather a better understanding, we took a closer look at the energetics (Figure S46). Three scenarios are taken into consideration. First, a direct charge transfer from BODIPY to  $\text{TiO}_2$ ; second, a charge transfer in terms of electrons from the (metallo)porphyrin to BODIPY; third a charge transfer in terms of electrons from BODIPY to the (metallo)porphyrin. Based on a previous report by our research group,<sup>[27]</sup> we rule out anchoring of the cyanurates to  $\text{TiO}_2$  and direct charge injection from BODIPY to  $\text{TiO}_2$ .<sup>[27]</sup> If a charge transfer from the (metallo)porphyrin to BODIPY would take place, such mechanism should be operative in solution studies as well. However, we could not gather any experimental evidence for this pathway. As such, we rule out any charge transfer from the (metallo)porphyrin to BODIPY. Upon closer inspection of the transient absorption spectra, signatures of the one-electron oxidized form of BODIPY are noted in the form of a broadened bleaching and an intensification of the 700 nm features. Both of them appear right after the conclusion of charge injection from the (metallo)porphyrin to  $\text{TiO}_2$  (Figure S45).<sup>[31]</sup> Full deconvolution of the latter is, however, difficult due to the overlap with the signatures of the one-electron oxidized form of the (metallo)porphyrin. In summary, we postulate for  $\text{TiO}_2$ -**9d-16** a charge transfer from BODIPY **16** to (metallo)porphyrin **9d** following the initial charge injection from (metallo)porphyrin **9d** into  $\text{TiO}_2$  as the *modus operandi*. **15-10c** shows no pronounced changes relative to **10c** film.

#### Application of orthogonally assembled bilayers in DSSC devices

Following earlier work,<sup>[27]</sup> the photovoltaic characteristics were investigated using a standard sandwich-type DSSC configuration comprised of a 9  $\mu\text{m}$  thick  $\text{TiO}_2$  layer as photoanode (Figures S48 and S49), a  $\text{I}^-/\text{I}_3^-$ -based electrolyte, and a platinum counter electrode—for more information please refer to the Supporting Information. In contrast to previous studies by our group,<sup>[27]</sup> we opted for a reverse ordering of the bilayer structure and used (metallo)porphyrins with different anchors to bind to the semiconducting  $\text{TiO}_2$  (Scheme 1).

First, devices featuring monolayers of **10c** ( $\text{TiO}_2$ -**10c**) and bilayers of **10c-15** ( $\text{TiO}_2$ -**10c-15**) were prepared and characterized. Current–voltage ( $J$ - $V$ ) assays were performed enabling first insights into the effect of post-functionalization on the device figures-of-merit, that is, efficiency ( $\eta$ ), fill factor (FF), short-circuit current ( $J_{\text{SC}}$ ), and open-circuit voltage ( $V_{\text{OC}}$ ) (Figure 5, top and Table 1). Importantly,  $\eta$  increased from 0.14% for  $\text{TiO}_2$ -**10c** to 0.16% for  $\text{TiO}_2$ -**10c-15** due to higher  $J_{\text{SC}}$ , namely 0.42 versus 0.46  $\text{mA cm}^{-2}$ . We rationalize our  $J$ - $V$  observation based on either a direct charge injection from BODIPY into  $\text{TiO}_2$  or a charge transfer from BODIPY to the (metallo)porphyrin (vide infra). To proof or disproof these two different pathways, IPCE (incident photon-to-current efficiency) measurements were performed. By virtue of the lack of additional features in the IPCE spectra seen for  $\text{TiO}_2$ -**10c-15**, a direct charge injection from BODIPY into  $\text{TiO}_2$  is very unlikely (Figure 5, bottom left). Consequently, the higher  $\eta$ s are in line with the TAS measurements (vide supra) attributed to the se-

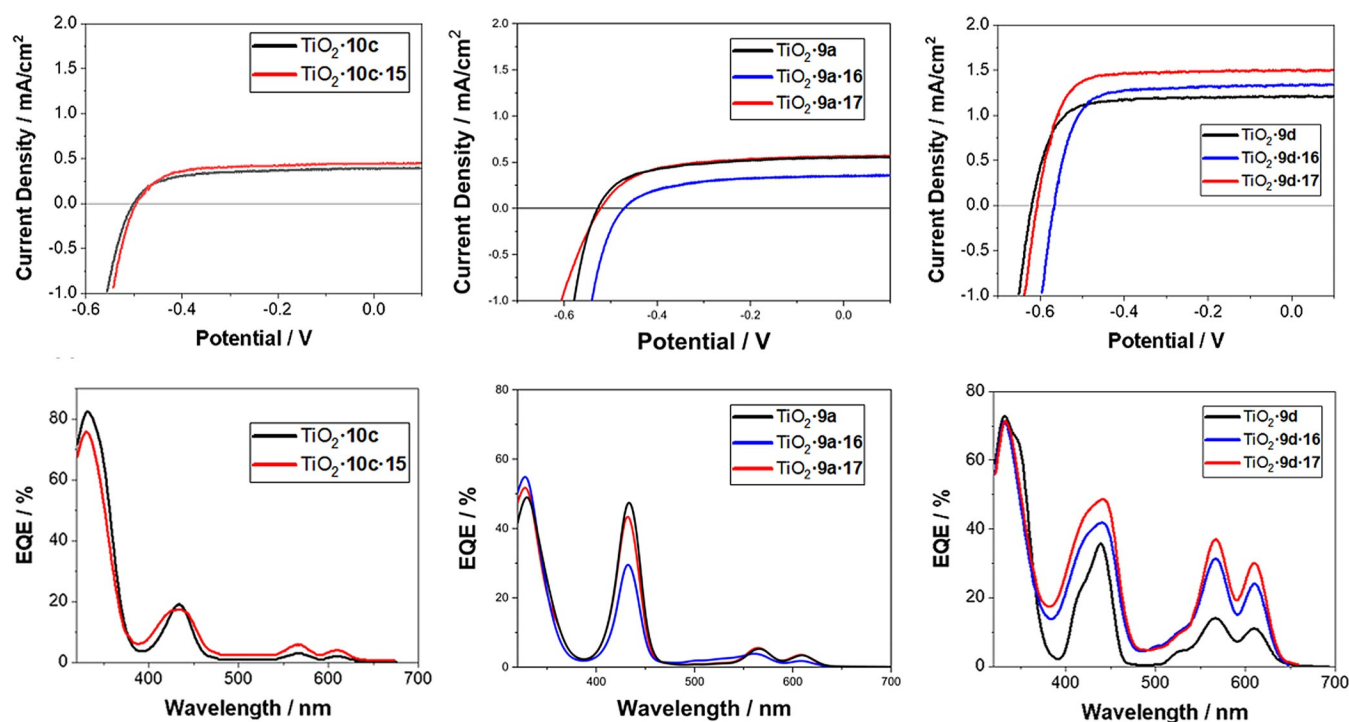


**Figure 5.** *J*-*V* assays (top) and IPCE measurements (bottom) of  $\text{TiO}_2$  devices:  $\text{TiO}_2\cdot 10\text{c}$  and  $\text{TiO}_2\cdot 10\text{c}\cdot 15$  (left),  $\text{TiO}_2\cdot 9\text{a}$ ,  $\text{TiO}_2\cdot 9\text{a}\cdot 16$ , and  $\text{TiO}_2\cdot 9\text{a}\cdot 17$  (middle), and  $\text{TiO}_2\cdot 9\text{d}$ ,  $\text{TiO}_2\cdot 9\text{d}\cdot 16$ , and  $\text{TiO}_2\cdot 9\text{d}\cdot 17$  (right).

Table 1. Summary of the devices' figures of merits.				
Dye combination	Efficiency [%]	FF [%]	$J_{\text{SC}}$ [ $\text{mA cm}^{-2}$ ]	$V_{\text{OC}}$ [V]
10c	0.14	65	0.42	0.51
15-10c	0.16	68	0.47	0.50
9a	0.20	62	0.62	0.52
9a-16	0.10	60	0.38	0.47
9a-17	0.19	60	0.60	0.51
9d	0.54	75	1.25	0.62
9d-16	0.61	74	1.43	0.57
9d-17	0.77	76	1.50	0.61

quence of charge injection from (metallo)porphyrin **10c** into  $\text{TiO}_2$  followed by charge transfer from BODIPY **15** to (metallo)porphyrin **10c**. Such a sequence assists in rationalizing the rather moderate increase in  $\eta$  and  $J_{\text{SC}}$ . A moderate increase in  $J_{\text{SC}}$  suggests one or more of the following scenarios as bottlenecks. First, the dicarboxylate anchor might potentially slow down or even hinder charge injection. Second, the positioning of the Hamilton receptor might shift the electron density away from the semiconducting surface. Third, the use of BODIPY in the post-functionalization might be inefficient in terms of charge injection.

To investigate the aforementioned series of devices, featuring monolayers of **9a** ( $\text{TiO}_2\cdot 9\text{a}$ ) or bilayers of **9a-16** and **9a-17** ( $\text{TiO}_2\cdot 9\text{a}\cdot 16$  and  $\text{TiO}_2\cdot 9\text{a}\cdot 17$ ), were prepared and characterized by means of *J*-*V* and IPCE assays. To this end, **9a** was synthesized with only a monocarboxylic ester anchor rather than a dicarboxylate anchor like in **10c** and a Hamilton receptor instead

of a cyanurate. Additionally, the post-functionalization includes BODIPY (**16**) as well as (metallo)porphyrin **17**. When comparing the figures-of-merit for  $\text{TiO}_2\cdot 9\text{a}$  with  $\text{TiO}_2\cdot 10\text{c}$ , a higher efficiency of 0.2% for  $\text{TiO}_2\cdot 9\text{a}$  rather than 0.14% for  $\text{TiO}_2\cdot 10\text{c}$  stem from different  $J_{\text{SC}}$ s: 0.62 versus 0.42  $\text{mA cm}^{-2}$ . The post-functionalization with **16** and **17** resulted, however, in lower  $\eta$ s of 0.1% and 0.19% for **9a-16** and **9a-17**, respectively. Lower  $\eta$ s are linked to lesser FFs,  $V_{\text{OC}}$ s, and  $J_{\text{SC}}$ s. The latter goes hand-in-hand with weaker contributions in the Soret-band region at around 430 nm in the IPCE measurements upon post-functionalization. A closer inspection of the devices following the measurements showed that the red-colored electrolyte turned bright green as a consequence of post-functionalization. This is taken as clear evidence for desorption from the semiconducting  $\text{TiO}_2$ . From the aforementioned we conclude that changing to a Hamilton receptor rather than a cyanurate affects  $\eta$ , but a monocarboxylic ester anchor leads to quick and quantitative desorption when post-functionalized.

To remedy this shortcoming,  $\text{TiO}_2\cdot 9\text{d}$  was prepared and tested in combination with  $\text{TiO}_2\cdot 16$  and  $\text{TiO}_2\cdot 17$ . **9d** is still a Hamilton receptor, but features unlike **9a** a dicarboxylate anchor. The figures-of-merit for  $\text{TiO}_2\cdot 9\text{d}$  taken from the *J*-*V* measurements show a  $V_{\text{OC}}$  of 0.62 V compared to 0.52 V determined for **9b**. This is attributed to a better surface coverage. Of even greater importance is, however, a  $J_{\text{SC}}$  of 1.25  $\text{mA cm}^{-2}$  for **9d**, which is with 0.62  $\text{mA cm}^{-2}$  double than that seen for  $\text{TiO}_2\cdot 9\text{a}$ . Accordingly,  $\eta$  for  $\text{TiO}_2\cdot 9\text{d}$  is 0.54%; please compare that to a  $\eta$  of 0.2% for  $\text{TiO}_2\cdot 9\text{a}$ . The main reason behind the  $J_{\text{SC}}$  changes is explained by the IPCE assays. Here, a broadening and an increase regarding contributions in the Soret- and Q-



band regions are noted for  $\text{TiO}_2\cdot\mathbf{9d}$  relative to the observations made for  $\text{TiO}_2\cdot\mathbf{9a}$  (Figure 5 middle and right).

Such a broadening is associated with stronger interactions with  $\text{TiO}_2$ . In turn, charge injection is facilitated and  $J_{\text{SC}}$  is increased. Next, we turned to devices based on bilayers of  $\mathbf{9d}\cdot\mathbf{16}$  and  $\mathbf{9d}\cdot\mathbf{17}$  and their characterization. Most important is the fact that  $\eta$  further increased from 0.54 % for  $\text{TiO}_2\cdot\mathbf{9d}$  to 0.61 % and 0.77 % for  $\text{TiO}_2\cdot\mathbf{9d}\cdot\mathbf{16}$  and  $\text{TiO}_2\cdot\mathbf{9d}\cdot\mathbf{17}$ , respectively. The (metallo)porphyrin post-functionalization, that is,  $\text{TiO}_2\cdot\mathbf{9d}\cdot\mathbf{17}$ , outperforms the BODIPY post-functionalization, that is,  $\text{TiO}_2\cdot\mathbf{9d}\cdot\mathbf{16}$ , by 26 %. The main cause is again an enhanced  $J_{\text{SC}}$ , most likely due to a charge transfer from  $\mathbf{16}$  and  $\mathbf{17}$  to  $\mathbf{9d}$ .

To summarize, all factors, that is, the use of a Hamilton receptor and its positioning, the post-functionalization as well as the respective anchor are critical in terms of maximizing the overall efficiencies. This highlights the necessity of a stable and robust anchor as well as a tailored self-assembly to generate high-performing devices. Building on the knowledge gathered through this work, higher overall efficiencies could be targeted through careful synthetic modifications of the first- and second layer dyes. In particular, a direct attachment of the supramolecular recognition motif and the carboxylate anchoring groups to the porphyrin moiety, as well as addition of strong electron donor groups, could lead to significantly higher efficiencies.

## Conclusions

In this work, we prepared a library of  $\text{AB}_2\text{C}$  (metallo)porphyrins featuring a stable anchoring group, on one hand, as well as a versatile supramolecular recognition motif, on the other hand. Additionally, we complemented the supramolecular recognition motif by designing corresponding porphyrins and BODIPYs. In a step-by-step fashion, we succeeded in binding the anchor to  $\text{TiO}_2$  nanoparticles and in employing a second dye layer via hydrogen bonding. In short, our coating strategy synergizes the benefits of a strong covalent anchoring of the first dye layer, that is, a (metallo)porphyrin, with the versatility of a non-covalently attaching a second dye layer, that is, either a (metallo)porphyrin or a BODIPY. Our investigations were, however, not only limited to solution studies but were matched with corresponding DSSC-based assays. Our studies demonstrated the importance of integrating the Hamilton receptor within the first dye layer and using a dicarboxylic acid anchor to prevent desorption from the  $\text{TiO}_2$  nanoparticles. To this end, highest DSSC efficiencies were noted when employing Hamilton receptor porphyrin  $\mathbf{9d}$  and  $\text{TiO}_2$  to afford  $\text{TiO}_2\cdot\mathbf{9d}$ . A non-covalent post-functionalization with either cyanuric acid BODIPY  $\mathbf{16}$  or cyanuric acid (metallo)porphyrin  $\mathbf{17}$  led to an increase in DSSC efficiency.  $\text{TiO}_2\cdot\mathbf{9d}\cdot\mathbf{17}$ , which turned out to be most effective bilayer, improved the DSSC efficiency by 43 %. A comprehensive understanding of the underlying mechanics came from transient absorption spectroscopy (TAS) measurements with the (metallo)porphyrin-BODIPY couples  $\mathbf{10c}\cdot\mathbf{15}$  and  $\mathbf{9d}\cdot\mathbf{16}$ . It is only in  $\text{TiO}_2\cdot\mathbf{9d}\cdot\mathbf{16}$  that the spectroscopic features of the one-electron oxidized form of the (metallo)porphyrin  $\mathbf{9d}$  and those of the one-electron oxidized BODIPY  $\mathbf{16}$  were observed. This suggests for  $\text{TiO}_2\cdot\mathbf{9d}\cdot\mathbf{16}$  an intramolecular charge-

transfer process from  $\mathbf{16}$  to  $\mathbf{9d}$  following the initial interfacial charge injection from  $\mathbf{9d}$  into  $\text{TiO}_2$ .

## Experimental Section

Full experimental details regarding the synthesis and characterization of all organic building blocks, electrochemical characterization, optical spectroscopy, and the preparation of DSSC devices are given in the Supporting Information.

## Acknowledgements

T.L. and A.Z. contributed equally to this work. We gratefully thank the Cluster of Excellence "Engineering of Advanced Materials" (EAM) funded by the German Research Council (DFG), the Bavarian collaborative research project "Solar Technologies go Hybrid (SolTech)", the Graduate School "Molecular Science" (GSMS) and the Graduate School "Advanced Materials and Processes" (GSAMP) for financial support. Additionally, we acknowledge the support of Dr. Fabian Lodermeier. Open access funding enabled and organized by Projekt DEAL.

## Conflict of interest

The authors declare no conflict of interest.

**Keywords:** dyes · hierarchical · sequential functionalization · solar cells · titania

- [1] a) J. Kao, K. Thorkelsson, P. Bai, B. J. Rancatore, T. Xu, *Chem. Soc. Rev.* **2013**, *42*, 2654–2678; b) C. Sanchez, B. Julián, P. Belleville, M. Popall, *J. Mater. Chem.* **2005**, *15*, 3559–3592; c) J. Yang, C.-H. Lee, H.-J. Ko, J.-S. Suh, H.-G. Yoon, K. Lee, Y.-M. Huh, S. Haam, *Angew. Chem. Int. Ed.* **2007**, *46*, 8836–8839; *Angew. Chem.* **2007**, *119*, 8992–8995; d) D. M. Guldi, G. M. A. Rahman, N. Jux, D. Balbinot, U. Hartnagel, N. Tagmatarchis, M. Prato, *J. Am. Chem. Soc.* **2005**, *127*, 9830–9838.
- [2] a) Q. M. Kainz, O. Reiser, *Acc. Chem. Res.* **2014**, *47*, 667–677; b) T. Luchs, P. Lorenz, A. Hirsch, *ChemPhotoChem* **2020**, *4*, 52–58; c) R. B. N. Baig, R. S. Varma, *Chem. Commun.* **2013**, *49*, 752–770.
- [3] a) Y. Kim, R. C. Johnson, J. T. Hupp, *Nano Lett.* **2001**, *1*, 165–167; b) L. Qin, G. Zeng, C. Lai, D. Huang, P. Xu, C. Zhang, M. Cheng, X. Liu, S. Liu, B. Li, H. Yi, *Coord. Chem. Rev.* **2018**, *359*, 1–31; c) L. Zeininger, S. Nagelberg, K. S. Harvey, S. Savagatrup, M. B. Herbert, K. Yoshinaga, J. A. Capobianco, M. Kolle, T. M. Swager, *ACS Cent. Sci.* **2019**, *5*, 789–795.
- [4] a) C. K. Kim, P. Ghosh, C. Pagliuca, Z.-J. Zhu, S. Menichetti, V. M. Rotello, *J. Am. Chem. Soc.* **2009**, *131*, 1360–1361; b) S. S. Agasti, A. Chompoosor, C. C. You, P. Ghosh, C. K. Kim, V. M. Rotello, *J. Am. Chem. Soc.* **2009**, *131*, 5728–5729.
- [5] a) M. Sarcelletti, D. Vivod, T. Luchs, T. Rejek, L. Portilla, L. Müller, H. Dietrich, A. Hirsch, D. Zahn, M. Halik, *Adv. Funct. Mater.* **2019**, *29*, 1805742; b) T. Luchs, M. Sarcelletti, L. Zeininger, L. Portilla, C. Fischer, S. Harder, M. Halik, A. Hirsch, *Chem. Eur. J.* **2018**, *24*, 13589–13595; c) X. Li, H. Lu, Y. Zhang, F. He, *Chem. Eng. J.* **2017**, *316*, 893–902.
- [6] B. O'Regan, M. Grätzel, *Nature* **1991**, *353*, 737–740.
- [7] a) M. Halik, A. Hirsch, *Adv. Mater.* **2011**, *23*, 2689–2695; b) L. Portilla, M. Halik, *ACS Appl. Mater. Interfaces* **2014**, *6*, 5977–5982; c) S. P. Pujari, L. Scheres, A. T. Marcelis, H. Zuilhof, *Angew. Chem. Int. Ed.* **2014**, *53*, 6322–6356; *Angew. Chem.* **2014**, *126*, 6438–6474; d) J. C. Love, L. A. Estroff, J. K. Kriebel, R. G. Nuzzo, G. M. Whitesides, *Chem. Rev.* **2005**, *105*, 1103–1170; e) P. J. Hotchkiss, S. C. Jones, S. A. Paniagua, A. Sharma, B. Kippelen, N. R. Armstrong, S. R. Marder, *Acc. Chem. Res.* **2012**, *45*, 337–346.

- [8] a) A. Jedaa, M. Salinas, C. M. Jäger, T. Clark, A. Ebel, A. Hirsch, M. Halik, *Appl. Phys. Lett.* **2012**, *100*, 063302; b) M. Burkhardt, A. Jedaa, M. Novak, A. Ebel, K. Voitchovsky, F. Stellacci, A. Hirsch, M. Halik, *Adv. Mater.* **2010**, *22*, 2525–2528.
- [9] M. Grätzel, *Acc. Chem. Res.* **2009**, *42*, 1788–1798.
- [10] G. E. Fryxell, P. C. Rieke, L. L. Wood, M. H. Engelhard, R. E. Williford, G. L. Graff, A. A. Campbell, R. J. Wiacek, L. Lee, A. Halverson, *Langmuir* **1996**, *12*, 5064–5075.
- [11] a) S. Mischler, S. Guerra, R. Deschenaux, *Chem. Commun.* **2012**, *48*, 2183–2185; b) S. H. Etschel, L. Portilla, J. Kirschner, M. Drost, F. Tu, H. Marbach, R. R. Tykwinski, M. Halik, *Angew. Chem. Int. Ed.* **2015**, *54*, 9235–9238; *Angew. Chem.* **2015**, *127*, 9367–9370; c) C. Haensch, S. Hoepfner, U. S. Schubert, *Chem. Soc. Rev.* **2010**, *39*, 2323–2334.
- [12] a) S. Mann, W. Shenton, M. Li, S. Connolly, D. Fitzmaurice, *Adv. Mater.* **2000**, *12*, 147–150; b) A. B. Descalzo, R. Martínez-Máñez, F. Sancenón, K. Hoffmann, K. Rurack, *Angew. Chem. Int. Ed.* **2006**, *45*, 5924–5948; *Angew. Chem.* **2006**, *118*, 6068–6093.
- [13] a) L. Zeininger, S. Petzi, J. Schönamgruber, L. Portilla, M. Halik, A. Hirsch, *Chem. Eur. J.* **2015**, *21*, 14030–14035; b) L. Zeininger, L. M. S. Stiegler, L. Portilla, M. Halik, A. Hirsch, *ChemistryOpen* **2018**, *7*, 282–287; c) L. M. S. Stiegler, T. Luchs, A. Hirsch, *Chem. Eur. J.* **2020**, *26*, 8483–8498; d) T. Pellegrino, L. Manna, S. Kuder, T. Liedl, D. Koktysh, A. L. Rogach, S. Keller, J. Rädler, G. Natile, W. J. Parak, *Nano Lett.* **2004**, *4*, 703–707.
- [14] a) S. Klein, T. Luchs, A. Leng, L. V. R. Distel, W. Neuhuber, A. Hirsch, *Bioengineering* **2020**, *7*, 126; b) S. Klein, L. M. S. Stiegler, C. Harreiss, L. V. R. Distel, W. Neuhuber, E. Spiecker, A. Hirsch, C. Kryschi, *ACS Appl. Bio Mater.* **2018**, *1*, 2002–2011.
- [15] G. Decher, *Science* **1997**, *277*, 1232–1237.
- [16] a) A. Burger, R. D. Costa, V. Lobaz, W. Peukert, D. M. Guldi, A. Hirsch, *Chem. Eur. J.* **2015**, *21*, 5041–5054; b) A. Burger, A. Kunzmann, R. D. Costa, R. Srikantharajah, W. Peukert, D. M. Guldi, A. Hirsch, *Chem. Eur. J.* **2018**, *24*, 7896–7905.
- [17] a) D. J. Broer, C. M. W. Bastiaansen, M. G. Debije, A. P. H. J. Schenning, *Angew. Chem. Int. Ed.* **2012**, *51*, 7102–7109; *Angew. Chem.* **2012**, *124*, 7210–7218; b) A. Ciesielski, C.-A. Palma, M. Bonini, P. Samori, *Adv. Mater.* **2010**, *22*, 3506–3520; c) V. Georgakilas, J. N. Tiwari, K. C. Kemp, J. A. Perman, A. B. Bourlino, K. S. Kim, R. Zboril, *Chem. Rev.* **2016**, *116*, 5464–5519.
- [18] a) S. K. Chang, A. D. Hamilton, *J. Am. Chem. Soc.* **1988**, *110*, 1318–1319; b) S. K. Chang, D. Van Engen, E. Fan, A. D. Hamilton, *J. Am. Chem. Soc.* **1991**, *113*, 7640–7645; c) V. Berl, M. Schmutz, M. J. Krische, R. G. Khoury, J.-M. Lehn, *Chem. Eur. J.* **2002**, *8*, 1227–1244; d) A. Ciesielski, G. Schaeffer, A. Petitjean, J.-M. Lehn, P. Samori, *Angew. Chem. Int. Ed.* **2009**, *48*, 2039–2043; *Angew. Chem.* **2009**, *121*, 2073–2077; e) G. Schaeffer, O. Fuhr, D. Fenske, J.-M. Lehn, *Chem. Eur. J.* **2014**, *20*, 179–186.
- [19] C. Dethlefs, J. Eckelmann, H. Kobarg, T. Weyrich, S. Brammer, C. Näther, U. Lüning, *Eur. J. Org. Chem.* **2011**, 2066–2074.
- [20] a) F. Wessendorf, A. Hirsch, *Tetrahedron* **2008**, *64*, 11480–11489; b) F. Wessendorf, B. Grimm, D. M. Guldi, A. Hirsch, *J. Am. Chem. Soc.* **2010**, *132*, 10786–10795.
- [21] A. Tron, P. J. Thornton, B. Kauffmann, J. H. R. Tucker, N. D. McClenaghan, *Supramol. Chem.* **2016**, *28*, 733–741.
- [22] S. Bosch, L. Zeininger, F. Hauke, A. Hirsch, *Chem. Eur. J.* **2014**, *20*, 2537–2541.
- [23] B. Grimm, J. Schornbaum, H. Jasch, O. Trukhina, F. Wessendorf, A. Hirsch, T. Torres, D. M. Guldi, *Proc. Natl. Acad. Sci. USA* **2012**, *109*, 15565–15571.
- [24] a) W. H. Binder, C. Kluger, M. Josipovic, C. J. Straif, G. Friedbacher, *Macromolecules* **2006**, *39*, 8092–8101; b) W. H. Binder, C. Kluger, C. J. Straif, G. Friedbacher, *Macromolecules* **2005**, *38*, 9405–9410.
- [25] L. Zeininger, M. Klamunzer, W. Peukert, A. Hirsch, *Int. J. Mol. Sci.* **2015**, *16*, 8186–8200.
- [26] M. Ali, D. H. Hasenöhrl, L. Zeininger, A. R. M. Müllner, H. Peterlik, A. Hirsch, *Helv. Chim. Acta* **2019**, *102*, e1900015.
- [27] L. Zeininger, F. Lodermeier, R. D. Costa, D. M. Guldi, A. Hirsch, *Chem. Commun.* **2016**, 52, 8842–8845.
- [28] < M. J. Plater, J. P. Sinclair, S. Aiken, T. Gelbrich, M. B. Hursthouse, *Tetrahedron* **2004**, *60*, 6385–6394.
- [29] T. Lazarides, G. Charalambidis, A. Vuillamy, M. Réglie, E. Klontzas, G. Froudakis, S. Kuhri, D. M. Guldi, A. G. Coutsolelos, *Inorg. Chem.* **2011**, *50*, 8926–8936.
- [30] J. Jiang, J. R. Swierk, K. L. Materna, S. Hedström, S. H. Lee, R. H. Crabtree, C. A. Schmuttenmaer, V. S. Batista, G. W. Brudvig, *J. Phys. Chem. C* **2016**, *120*, 28971–28982.
- [31] S. Aute, P. Maity, A. Das, H. N. Ghosh, *New J. Chem.* **2017**, *41*, 5215–5224.

Manuscript received: November 12, 2020

Revised manuscript received: January 7, 2021

Accepted manuscript online: January 11, 2021

Version of record online: February 15, 2021